

Megadunes in Antarctica: migration and characterization from remote and in situ observations

Giacomo Traversa^{1, 2}, Davide Fugazza³ and Massimo Frezzotti⁴

5 ¹ Institute of Polar Sciences, National Research Council of Italy, 20125 Milano, Italy

² Department of Physical Sciences, Earth and Environment (DSFTA), Università degli Studi di Siena, 53100 Siena, Italy

³ Department of Environmental Science and Policy (ESP), Università degli Studi di Milano, 20133 Milan, Italy

⁴ Department of Science, Università degli Studi Roma Tre, 00146 Rome, Italy

10 *Correspondence to:* Giacomo Traversa (giacomo.traversa@isp.cnr.it) and Massimo Frezzotti (massimo.frezzotti@uniroma3.it)

Abstract. Megadunes are peculiar features formed by the interaction between atmosphere and cryosphere and are known to be present only on the East Antarctic plateau and other planets (Mars and Pluto). In this study, we have analysed the 15 glaciological dynamic of megadunes, their spectral properties and morphology on two sample areas of the East Antarctic plateau where in the past international field activities were carried out (EAIIST and It-ITASE). Using satellite images spanning 7 years, we analysed the spatial and temporal variability of megadune surface characteristics, i.e., near infrared (NIR) albedo, thermal brightness temperature (BT) and Slope along the Prevailing Wind Direction (SPWD), useful for mapping them. These 20 parameters allowed us to characterise and perform an automated detection of the glazed surfaces, and we determined the influence of the SPWD by evaluating different combination of these parameters. The inclusion of the SPWD significantly increased the accuracy of the method, doubling it in certain analysed scenes. Using remote and field observations, for the first time we surveyed all the components of upwind migration (absolute, sedimentological and ice flow), finding an absolute value 25 of about 10 m a^{-1} . The analysis shows that the migration is driven by the snow accumulation on the crest and through prograding upwind on the previous windward flanks characterised by glazed surface. Our results present significant implications for Surface Mass Balance estimation, paleoclimate reconstruction using ice cores and for the measurements using optical and radar images/data in the megadune areas.

1 Introduction

Antarctic climate and mass balance have been highlighted by the Special Report on the Ocean and Cryosphere in a Changing Climate (Meredith et al., 2019) by the Intergovernmental Panel on Climate Change (IPCC) among the main uncertainties for 30 the climate system and sea level projections. Surface mass balance (SMB) is the net balance between the processes of snow precipitation and loss on a glacier surface and provides mass input to the surface of the Antarctic Ice Sheet. Therefore, it represents an important control on ice sheet mass balance and resulting contribution to global sea level change. Ice sheet SMB varies greatly across multiple scales of time (hourly to decadal) and space (metres to hundreds of kilometres), and it is

notoriously challenging to observe and represent in atmospheric models (eg. Agosta et al., 2019; Lenaerts et al., 2019).

35 Moreover, given the difficulties in accessing the interior of the ice sheet, only limited field observation on past and current conditions exists. The Southern part of the East Antarctic Ice Divide, from Concordia and Vostok Stations to the South Pole is the coldest and driest area on Earth and presents unique features called megadunes, which extend for more than 500,000 km² (Fahnestock et al., 2000). The drivers of megadune formation are uncommon snow accumulation and redistribution processes driven by wind scouring that remain relatively unexplained (Fahnestock et al., 2000; Frezzotti et al., 2002a, b; 40 Courville et al., 2007; Scambos et al., 2012; Dadic et al., 2013; Ekyakin et al., 2015, Fig. 1). Ground surveys of megadunes show that snow is removed from their leeward slopes where a specific erosional type of snow, “glazed surface” or “wind crust”, is formed as a result. In contrast, snow accumulation is increased on the windward slopes that are characterised by the depositional types of the snow microrelief termed “sastrugi”. Glazed surfaces form because wind and sublimation can ablate much more snow/firn than is accumulated by annual solid precipitation, causing a persistent SMB close to zero or negative. 45 The stability of climatic conditions could play a key role in megadune formation, since snow precipitation is very low while katabatic wind intensity and direction are stable; these conditions affect snow sintering and a high grade of snow metamorphism (Albert et al., 2004; Courville et al., 2007; Scambos et al., 2012; Dadic et al., 2013). Megadunes are oriented perpendicular to the Slope along the Prevailing Wind Direction (SPWD), wave amplitudes are small (up to 8 m), wavelengths range from 2 to over 5 km and megadune crests are nearly parallel, extending from tens to hundreds of kilometres 50 (Swithinbank, 1988; Fahnestock et al., 2000; Frezzotti et al., 2002a, b; Arcone et al., 2012a, b). The angle between the katabatic wind direction and the direction of general surface slope at a regional scale can differ up to 50° due to the interaction between the topographic slope driving gravity and the Coriolis force (Fahnestock et al., 2000; Frezzotti et al., 2002b).

Based on previous studies, the SMB of megadunes ranges between 25% (leeward faces glazed surfaces) and 120% (windward faces, covered by huge sastrugi up to 1.5 m in height) of accumulation in adjacent non-megadune areas (Frezzotti et al., 2002b).

55 The sedimentary structure of buried megadunes examined via Ground Penetrating Radar (GPR) and Global Position System (GPS) suggests that the sedimentary morphology of the windward face (sastrugi) migrates upwind with time, burying the glazed surface of the leeward face (Frezzotti et al., 2002b; Ekyakin et al., 2015), with typical “antidune” processes similar to those observed on fluvial and ocean bedforms (Prothero and Schwab, 2004). This uphill migration is caused by the difference in accumulation between windward (high accumulation) and leeward (near-zero or negative accumulation) sides, also leading 60 to differences in snow features and surface roughness (Fahnestock et al., 2000; Frezzotti et al., 2002a; Albert et al., 2004; Courville et al., 2007). Megadunes appear to be formed by an oscillation in the katabatic air flow, leading to a wave-like variation in net accumulation; the wind-waves are formed at the change of SPWD, in response to the buoyancy force, favouring the standing-wave mechanism (Fahnestock et al., 2000; Frezzotti et al., 2002b). According to Dadic et al. (2013), who based 65 his analysis on superficial-flow theory for sediments in water (Núñez-González and Martín-Vide, 2011) and atmospheric flow modelling, persistent katabatic winds, strong atmospheric stability and spatial variability in surface roughness are the primary controllers of upwind accumulation and migration of megadunes, where the latter represents the main factor that influences their velocity.

The surface waveforms of megadunes with regular bands of sastrugi and glazed surfaces allow surveying the megadunes by satellite observations, because of differences in albedo and microwave backscatter (Fahnestock et al., 2000; Frezzotti et al., 2002a; Scambos et al., 2012) between these features and surrounding snow. Spectral differences also lead to an effect on temperatures, which is on average higher than on the snow surface (Fujii et al., 1987). In spite of the importance of the glazed surfaces of megadunes for the SMB of Antarctica, a remote sensing characterization of their physical properties and spatial distribution, and a quantitative analysis of their migration is currently lacking. The aim of the study is to provide a detailed survey of the spatial and temporal variability of two megadune areas using remote sensing data (Landsat 8 and Sentinel-2), high resolution elevation models (Reference Elevation Model of Antarctica REMA, Howat et al., 2019) and climatic conditions using atmospheric reanalysis data (ERA5) in addition to past in-situ measurement data (firn core, GPR and GPS), to explore spectral, thermal, and windward slope relationships with a view towards generating an algorithm for their automatic detection. Moreover, we provide for the first time the first measurements of the absolute megadune movement, and its different components: ice-flow and sedimentological progradation. The analysis of absolute megadune movement has important implications on the remote sensing ice dynamic measurements, in particular on ice flow measurements and elevation changes. Our work constitutes substantial progress towards the survey of ablation areas on SMB at small spatial scales over ice sheets using surface morphology (SPWD) and albedo detection by satellite. A clear understanding of these interactions is of primary importance for the climatic interpretation of ice records and for the assessment of processes and rates of wind scouring and its SMB implications.

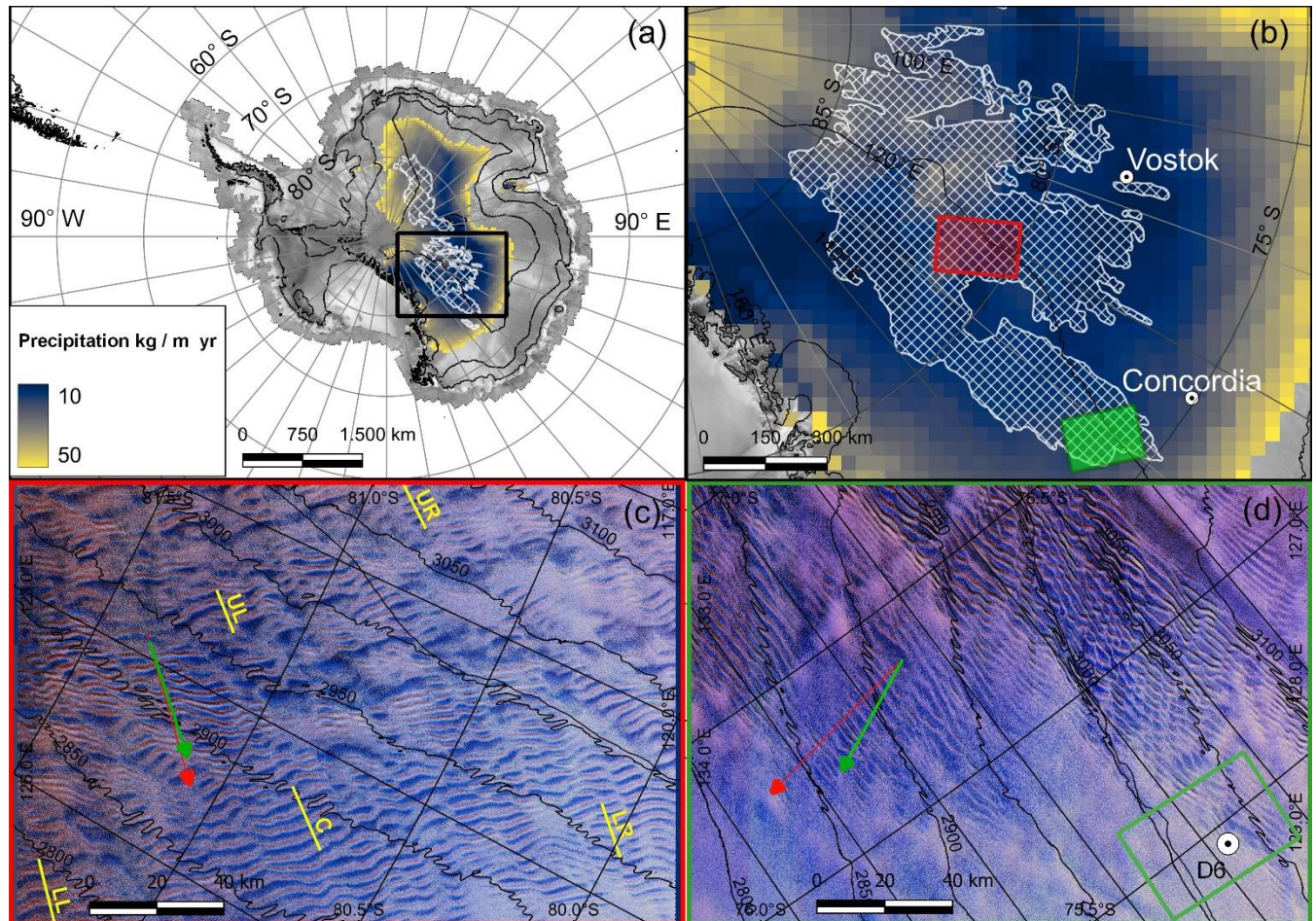
1.1 Study area

Megadune fields on the Antarctic continent extend along 10° in latitude (75° - 85° S, about 1100 km) and 30° in longitude (110° - 140° E, about 300-600 km). The climatic conditions of the area are characterised by extremely low temperatures (mean annual temperatures from -45° to -60° C), extremely low snow precipitation (<30 mm water equivalent per year, w.e.a $^{-1}$; Van Wessem et al., 2014; Agosta et al., 2019) and nearly constant katabatic wind direction and wind speed (6 - 12 m s $^{-1}$; Courville et al., 2007).

Analysis of data acquired by the Cloud-Aerosol Lidar and Infrared Pathfinder Satellite Observation (CALIPSO) satellite has enabled the construction of a 12-year climatology of blowing snow over Antarctica, showing that the greatest frequency of blowing snow events, approaching 75% of observations, is seen in the megadune region (Palm et al., 2019).

This research focuses on two megadune areas that were crossed and surveyed by two snow traverse expeditions: EAIIST (East Antarctic International Ice Sheet Traverse) in 2018-19 and It-ITASE (Italian-International TransAntarctic Scientific Expedition) in 1998-1999. EAIIST area is situated 300 km East of Vostok Station (centred at $80^{\circ}47'$ S $122^{\circ}19'$ E) and It-ITASE area 150 km East of Concordia Station (centred at $75^{\circ}54'$ S $131^{\circ}36'$ E; Fig. 1). The survey data of the first area (EAIIST, <https://www.eaiist.com/en/>) are under processing whereas the *in situ* observations of the second traverse It-ITASE are available (Frezzotti et al., 2002a, b, 2004, 2005; Proposito et al., 2002; Vittuari et al., 2004). The EAIIST area is in the middle of the megadune area; thus, megadunes are well defined and continuous on satellite images in optical and microwave bands, whereas the It-ITASE area is at the North-East limit of the megadune field where this morphology is discontinuous and disappears,

thus representing the developing threshold of the environmental conditions (morphology, climatology, glaciology) determining megadune formation.



105 **Figure 1: Location map of megadune area:** (a) Satellite image map of the Antarctic continent (Jezek, 1999) with elevation contour lines at 1000 m a.s.l. intervals, megadune regions are shown as cross-hatched white areas (Fahnestock et al., 2000), with snow precipitation by RACMO in colour for areas with precipitation $< 50 \text{ kg m}^{-2} \text{ a}^{-1}$ (Van Wessem et al., 2014), black rectangle (b box).
110 (b) The megadune field with two study sites, EAIIST red rectangle (c box) and It-ITASE green rectangle (d box). (c) Landsat 8 OLI image in false colour (069119 scene, 17/Dec/2015) of the EAIIST area. (d) Landsat 8 OLI image in false colour (081114 on 18/Dec/2014) of the It-ITASE area and D6 core site; the green rectangle shows the location of Fig. 4. In (c) and (d) boxes, red arrows represent ERA5 wind direction and green arrows sastrugi-based wind direction, while the yellow lines show the location of the transects studied.

Topographically, the two study areas are in a relative sloping zone where the altitude decreases moving from SW to NE and the elevation ranges from 2700 to 3200 m a.s.l. Thus, the topographic aspect (the direction that a topographic slope faces) is generally East (~ 80°, It-ITASE and ~ 70°, EAIIST). The regional topographic slope (10 km scale) is on average 1.5 m km⁻¹ and 1.8 m km⁻¹ for the It-ITASE and EAIIST areas, respectively. The katabatic wind direction is nearly constant with wind blowing from SW in both areas.

2 Data and Methods

2.1 Data

In order to study the megadune areas, we combined three main datasets (satellite images, meteorological data from reanalysis products, DEM) to create a method for the automatic detection of snow glazed surfaces. We tested two methods, one by creating 5 sample transects in the EAIIST area (Fig. 1c) and visually identifying thresholds of albedo, thermal brightness temperature (BT) and SPWD to discriminate between glazed surfaces and surrounding snow. The 5 transects were created in different areas of the megadune field and they show relatively different wind directions and topographic aspect and slope, with the aim of representing the widest possible range of SPWD values. For the second method, i.e. a maximum likelihood supervised classification, we created 30 polygons in the glazed snow area and 30 for firm, which were used to train the classification algorithm.

2.1.1 Satellite datasets

Two sources of satellite imagery were used: Landsat 8 OLI satellite images and Sentinel-2 images, both downloaded from the Earth Explorer portal (<https://earthexplorer.usgs.gov/>). Landsat 8 OLI and Sentinel-2 provide data in several spectral bands, including panchromatic, visible, very near infrared, short-wave infrared, and thermal infrared bands, with different spatial resolution from 10 to 100 m. Satellite images from Landsat 8 OLI (supplementary Table A1) were chosen at dates close to the first stripe acquisitions of the REMA DEM (2013, Table A2). The megadune area is subject to blowing snow events (more than 75% of the time; Palm et al, 2019) and cloud cover. Moreover, in the morning a strong atmospheric inversion layer develops 70 % of the time during summer on the Antarctic plateau (Pietroni et al., 2014) with the formation of fog, which is not homogeneously distributed on the area surveyed by satellite images and is difficult to detect. Therefore, we excluded from our dataset all images with cloud cover > 10% of land surface, visible blowing snow and fog events and images with solar zenith angle (SZA) $\geq 75^\circ$ (because of the effect on the albedo, as demonstrated by Picard et al., 2016), and obtained 17 images from Landsat 8 from 2013 to 2020 and 4 images from Sentinel-2 from 2018 to 2021 (Table A1), 11 for the EAIIST site and 6 for It-ITASE. To map glazed surfaces on megadunes, we used Landsat 8 OLI data as the method relies on the calculation of the albedo, which has been thoroughly validated for Landsat 8 OLI (Traversa et al., 2021a). Additionally, Landsat 8 OLI is available for a longer period of time compared to Sentinel-2, allowing us to investigate temporal evolution of the megadune area. In the megadune area, the difference between snow glazed surfaces and snow is higher considering NIR spectral albedo

145 and BT (Traversa et al., 2021b). To a “higher” amount of solar radiation absorbed by the glazed surface, corresponds also a different BT on snow glazed surfaces (Fujii et al., 1987; Scambos et al., 2012 and references therein). In fact, these zones show a higher BT compared to the upwind part of the dune characterised by the snow surface. In detail, we used Landsat 8 OLI Near InfraRed band (NIR band 5, with a ground resolution of 30 m) to calculate NIR albedo and thermal infrared (TIRS 1) band 10 to calculate BT (with a ground resolution of 100 m, provided resampled to 30 m). To perform the megadune migration analysis
150 (sect 2.2.2), we used the panchromatic band of Landsat 8 OLI, as this band has a higher resolution (15 m) compared to the other spectral bands of Landsat. For comparison, Sentinel-2 images were also used, specifically Band 8 NIR (10 m spatial resolution), which allows better observing differences between snow and glazed surfaces compared to the other visible and infrared bands.

155 **2.1.2 Atmospheric reanalysis dataset**

We extracted wind direction from the ERA5 atmospheric reanalysis global climate dataset (Hersbach et al., 2020) and by identification of sastrugi based on Landsat (Sect. 2.2.1). In particular, we used ERA5 *hourly data* (DOI: 10.24381/cds.adbb2d47) of wind speed and direction at 10 m above the surface averaged over a 20-year temporal period, from 2000 to 2019. Beside using all wind speed observations, we further divided wind speed in 5 classes, only considering wind speed values above specific thresholds, i.e., wind speed $>3 \text{ m s}^{-1}$, $>5 \text{ m s}^{-1}$, $>7 \text{ m s}^{-1}$ and $>11 \text{ m s}^{-1}$. These thresholds were chosen based on the interactions between wind and snow: snow transportation by saltation (within 0.3 m in elevation) starts at wind speeds between 2 and 5 m s^{-1} , transportation by suspension (drift snow) starts at velocities $> 5 \text{ m s}^{-1}$ (within 2 m) and blowing snow (snow transportation higher than 2 m) starts at velocities between 7 and 11 m s^{-1} (see Frezzotti et al., 2004 and references therein). The threshold wind speed at which the sublimation of blowing snow starts to contribute substantially to
160 katabatic flows in a feedback mechanism appears to be 11 m s^{-1} (Kodama et al., 1985; Wendler et al., 1993).

165 **2.1.3 Topographic dataset (DEM)**

In order to obtain the aspect and slope of the surface for the SPWD calculation and perform topographic correction for the calculation of albedo, we used a mosaic of REMA tiles (www.pgc.umn.edu/data/rema/; Howat et al., 2019). These are constructed from thousands of individual stereoscopic Digital Terrain Models (DEMs) at high spatial resolution (8 m). Each
170 individual DEM was vertically registered to satellite altimetry measurements from Cryosat-2 and ICESat, resulting in absolute uncertainties of less than 1 m, and relative uncertainties of decimetres. REMA is based mainly on imagery acquired during the austral summer period (December-March) and at the two sites, the temporal period is from 2008 to 2017, although 87.5% of stripes were acquired in 2013-2017 (Table A2).

2.2 Methods

175 The study includes four main processing steps: Landsat 8 OLI image processing for the calculation of NIR albedo; extraction of thermal BT from the Landsat thermal band 10; SPWD calculation from ERA5 and satellite sastrugi-based wind direction,

estimation of the surface velocity and migration of megadunes using feature tracking (2014-2021) and comparison of GPR-GPS measurements from 1999 with the REMA DEM from 2014 (specific strip on the area). The first three steps were at the basis of the automatic detection of the snow glazed areas.

180 **2.2.1 Automatic detection of glazed snow surfaces**

By using spectral datasets and topographic data, we consider for the automatic detection of the glazed areas the following parameters: NIR albedo, thermal BT and SPWD. NIR albedo (α), was here estimated using Landsat 8 OLI imagery, following the method first proposed by Klok et al. (2003) and recently tested and validated in Antarctica by Traversa et al. (2021a). We used NIR albedo as opposed to broadband albedo owing to the higher detection ability of NIR albedo, which stems from the fact that broadband albedo obtained by using Liang conversion algorithm (Liang, 2001) considers the visible area of the spectrum and the shortwave infrared. In fact, in broadband albedo it is hardly possible to recognize the differences between glazed and unglazed areas, which in the visible wavelengths look very similar (Warren, 1982).

185 Following the methodology proposed by Traversa et al. (2021a, c), the images were processed through three main steps: 1) conversion of radiance to Top of Atmosphere (TOA) reflectance by using per-pixel values of the SZA available through the Landsat solar zenith band. This conversion allows applying a more accurate per-pixel correction for the SZA, useful in our study considering the average high SZA (always $\geq 59^\circ$, Table A1), and its strong effect on albedo (Pirazzini, 2004; Picard et al., 2016; Traversa et al., 2019); 2) atmospheric correction; 3) topographic correction.

190 To retrieve the thermal BT, we employed band 10 of Landsat 8. To estimate the TOA thermal BT received at the satellite, spectral radiance in the thermal band was converted using the thermal constants in the Landsat metadata (Zanter, 2019).

195 For the SPWD, the wind directions were extracted at low spatial resolution (30 km) using ERA5 and validated by identifying sastrugi and deriving wind directions from them using Landsat 8 OLI at 30 m spatial resolution (Mather, 1962; Parish and Bromwich, 1991). The identification of sastrugi was performed on the Landsat 8 OLI NIR band (band 5) by applying the Canny edge detection algorithm (*i.edge* in GRASS GIS, Canny, 1986). Prior to edge detection, each image was pre-processed by using a high pass filter with a length scale of 150 m implemented through a Fast Fourier Transform to highlight the sastrugi.

200 This process was applied on 7 Landsat scenes from the spring and summer months i.e., November, December and January of the period 2013-2020.

To further estimate the SPWD based on the wind direction from ERA5 and Landsat-derived sastrugi, we used the approach of Scambos et al. (2012), i.e., we calculated the dot product between the slope derived from the REMA DEM and the wind direction. The algorithm was applied to ERA5 and sastrugi-based wind directions resampled at 120 m spatial resolution, and 205 the REMA DEM was resampled to match ERA5 and sastrugi-based wind directions using bilinear interpolation. The resulting SPWD has units of m km^{-1} .

Due to the small difference in NIR albedo and BT of glazed surfaces (leeward) and sastrugi (windward) and the different illumination and meteorological conditions of the satellite images, the analysis of the variability of SPWD, NIR albedo and BT was conducted in detail on the five transects perpendicular to megadunes. The comparisons were conducted using the

210 albedo and temperature values and normalised using mean and standard deviation for each transect. Moreover, we determined
the strength of the relationship between SPWD vs NIR albedo, and SPWD vs thermal BT (applied on the moving averages of
11 pixels weighted based on the distance from the central point) using linear regression. The comparison analysis was
conducted at seasonal scale for the 2013-2014 (4 images) and at multi-annual scale on 17 images distributed over 8 years.
215 With the aim of providing an automatic methodology for distinguishing the glazed snow from the surrounding firn surface and
evaluate the role of SPWD in the classification, we applied and compared two different approaches: a supervised classification
(maximum likelihood) and a self-defined-threshold approach. In both cases, we considered SPWD, NIR albedo and thermal
BT. The analysed images were the one from 17-Dec-2015, which was one of the best available images in terms of cloud cover
(~0%), presenting no blowing snow/fog and the lowest SZA (67°) for the EAIIST site and the closest date to the REMA DEM
in the area (January-October 2016), and the four scenes available for the 2013-2014 season (i.e., 25-Nov-2013, 11-Dec-2013,
220 27-Dec-2013 and 28-Jan-2014). For the self-defined-threshold method, we applied a conditional calculation to automatically
map glazed snow. The thresholds were defined as follows: NIR albedo < 0.82 , thermal BT $> 246.5^\circ$ K and SPWD $> 1 \text{ m km}^{-1}$.
225 In order to evaluate the role of each parameter, with a particular attention to the SPWD, we repeated the two approaches by
using individual parameters (NIR, SPWD, BT) and combinations of them (i.e., NIR-SPWD, NIR-BT, BT-SPWD and NIR-
BT-SPWD). Finally, we calculated the accuracy for each case, by creating a set of random points (100 points, following the
density used in Azzoni et al., 2016) as ground truth (visually assigned on the false colour image) and comparing the results
through a confusion matrix. The accuracy was calculated both for methodologies in their entirety (identifying and
distinguishing glazed snow and the surrounding firn surface), but also with respect to their specific ability in detecting glazed
snow.

2.2.2 Megadune movement estimation

230 Frezzotti et al. (2002b) and Ekyakin et al. (2015), based on the sedimentary structure of buried megadunes (using GPR and
GPS), pointed out that the megadune migration and ice sheet surface flow show a similar intensity but opposite directions and
that megadunes migrates upwind with time, burying the glazed surface of the leeward face.
235 Here, by using different satellite images and field data, we are able to provide and quantify megadune migration components:
ice-flow (\vec{If}) direction, which is correlated mainly to topographic slope, sedimentological migration (\vec{M}_s), caused by
sedimentological processes linked to deposition (on the upstream dune flank) and ablation (on the downstream dune flank) of
snow, and the result of these processes, the absolute migration (\vec{M}_a):

$$\vec{M}_a = \vec{M}_s + \vec{If} \quad (1)$$

240 During the It-ITASE traverse at the D6 site, megadunes were surveyed by means of GPR-GPS to measure ice velocity, surface
elevation and internal layering of present and buried megadunes. We compared these measurements with the REMA DEM
derived by satellite images acquired in 2014 to estimate the change in surface morphology due to sedimentological migration
of the megadunes. With the aim of calculating the surface velocity and direction of megadune movement, the feature tracking

module *IMCORR* (Fahnestock et al., 1992; Scambos et al., 1992) was run in *System for Automated Geoscientific Analyses* (SAGA GIS). This algorithm performs image correlation based on two images providing the displacement of each pixel between the second and first image (Jawak et al., 2018). Prior to feature tracking, each image pair was pre-processed by using a low pass filter with a length scale of 150 m implemented through a Fast Fourier Transform to smooth out the sastrugi and leave megadune features for tracking. Finally, by dividing the displacement values obtained through *IMCORR* by the corresponding time period, we obtained the absolute migration of the megadunes in m a^{-1} . For comparison, we also employed another method to evaluate the megadune migration. By using Landsat 8 OLI imagery, similarly to what already done for the detection of sastrugi and applying an edge detection on band 5 (NIR), it is possible to identify the megadune crest and trough at the edges between leeward (glazed snow) and windward (sastrugi) zones. The obtained direction raster was manually cleaned from errors and artefacts (angles $< 200^\circ$ and $> 240^\circ$, intensity $< 5 \text{ m a}^{-1}$), and then vectorized after thinning, i.e., reducing the number of cells used to represent the width of the features to 1 pixel. Comparing the obtained velocity fields in different years, we could observe the absolute migration of the megadunes.

We considered the widest temporal interval between two pairs of cloud-free images of Landsat 8 (4 pairs) and Sentinel-2 (2 pairs), that were in a similar period of the year, to avoid relevant differences in the SZA that could confound the feature tracking algorithm (Table 1).

Zone	Satellite	t_0	t_1	t span (a)	Mean $M_a(\text{m a}^{-1})$	STD $M_a(\text{m a}^{-1})$	Features
It-ITASE	L8	02-Dec-2014	30-Nov-2019	5	14.0	3.9	30073
It-ITASE	L8	02-Dec-2014	02-Dec-2020	6	12.8	3.4	30538
It-ITASE	S2	13-Dec-2016	27-Dec-2020	4	11.4	3.8	537304
EAIIST	L8	27-Dec-2013	28-Dec-2019	6	11.9	3.6	316951
EAIIST	L8	17-Dec-2015	30-Dec-2020	5	14.2	3.4	139622
EAIIST	S2	10-Jan-2018	02-Jan-2021	3	10.5	4.1	1329648

Table 1. Results of the absolute migration of megadunes calculated from *IMCORR* based on Landsat 8 OLI (L8) and Sentinel-2 (S2) imagery at the It-ITASE and EAIIST sites.

The results from *IMCORR* and GPS observations were compared with the *MEaSUREs ice-flow velocity* product (Rignot et al., 2017), that provides the highest-resolution (450 m) digital mosaic of ice motion in Antarctica (assembled from multiple satellite interferometric synthetic-aperture radar systems, mostly between 2007-2009 and 2013-2016), showing for each pixel the direction and the velocity of ice flow with a mean error of 3-4%.

3 Results

3.1 Megadune characterization and automatic detection

265 On average, in the five analysed transects NIR albedo ranges from 0.81 to 0.86 (α) in the upwind area (snow sastrugi) and from 0.73 to 0.81 (α) downwind (glazed surfaces), with differences inside the transects of about 0.07 (α) with a maximum value of 0.1 (α). The maximum contrast of NIR albedo between glazed surfaces and snow sastrugi usually occurs at springtime (October-November) and decreases during the summer season (Fig. 2). Our remote sensing observations agree with previous analysis that pointed out that in late summer, radiative cooling of the uppermost surface layer leads to formation of a surface
270 frost, by condensation of local atmospheric vapour onto the snow surface; this gives the glazed surface a more diffuse specular reflection than in spring and changes its appearance in albedo and BT (Scambos et al., 2012 and references therein). Along the transects, the correlation of NIR albedo from the different images is high (R^2 up to 0.99) during the spring season (24 Nov 2013, 27 Dic 2013) and decreases by the end of the summer and in comparison with the following years, with an R^2 of 0.7 only after 2 years (17 Dec 2015) and up to 0.6 after 6 years (Dec 2019). A Similar decrease in correlation occurs from the
275 comparison of the SPWD and NIR albedo from 2013 (R^2 0.66) to 2019 (R^2 0.39).

For the thermal BT, we observed an intra-seasonal trend on all transects: in fact, while thermal BT remains ≥ 244 K during the middle of the summer (11-Dec-2013 and 27-Dec-2013), it decreases moving away from the summer solstice. Temperatures range between 238 K and 240.5 K on 25-Nov-2013, 26 days from the solstice. The difference increases on the date farthest from the solstice, 28-Jan-2014 (38 days from the solstice), with the lowest values ranging between 236 K and 239 K. The BT
280 varies up to 1.5 K for each transect, but up to 3-4 K within individual images. Intra-annually, the difference between glazed surfaces and snow is higher during the spring (max 1 K in November) and tends to decrease over time, becoming lower than 0.5 K at the end of summer (January), where differences between the two surfaces are hardly detectable and the correlation between the two parameters frequently decreases drastically. These differences are directly correlated to the ones observed in NIR albedo, as a higher quantity of energy is absorbed on glazed surfaces.

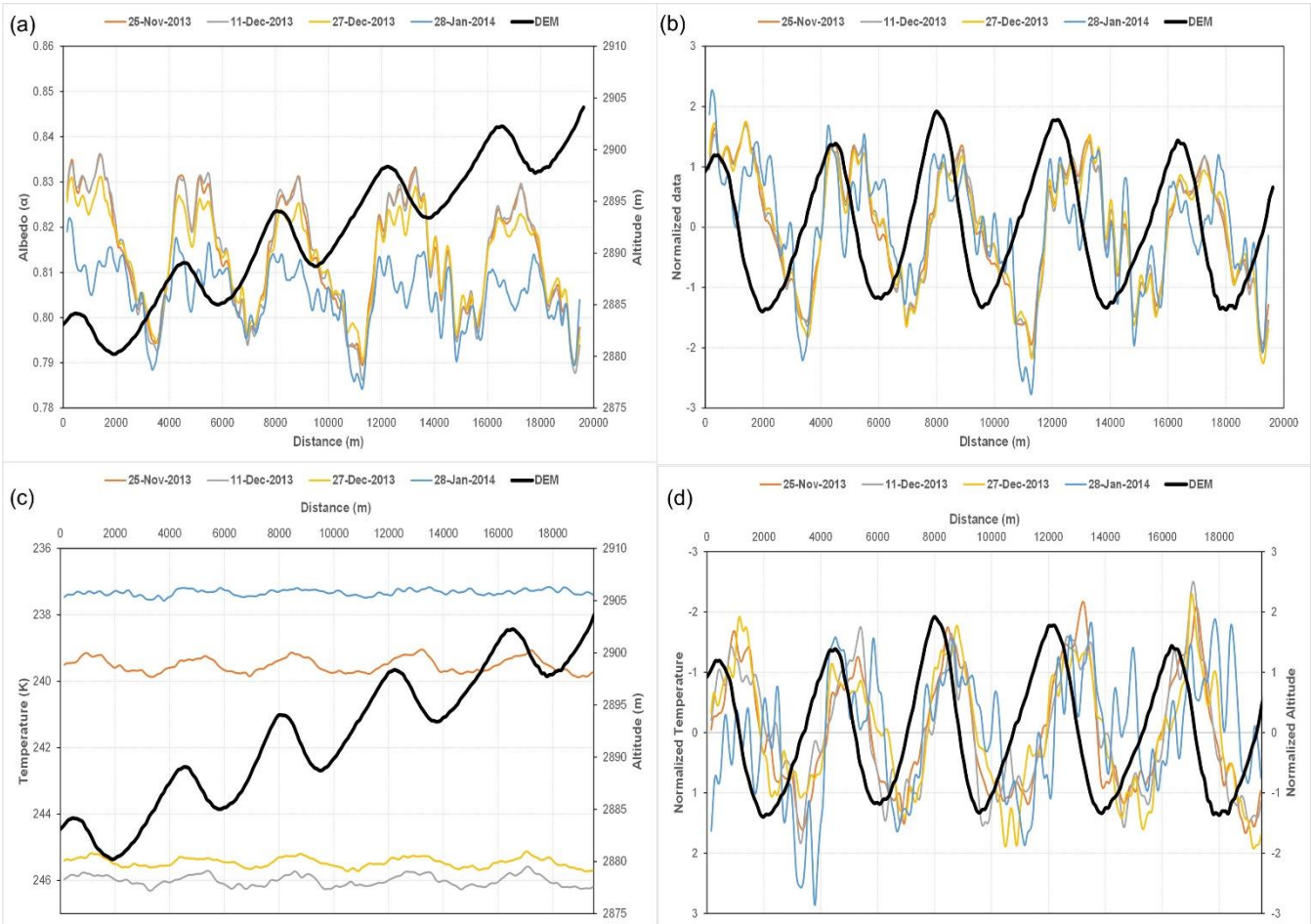


Figure 2: (a) moving average (based on 11 transect pixels) of NIR albedo (a) between November 2013 and February 2014 for transect C at the EAIIST site (see Fig. 1c for location) and elevation from REMA DEM. Corresponding normalised moving average of NIR albedo (b) and thermal BT TIRS1 (c) during the austral summer season 2013-2014 for transect C and elevation from REMA DEM (detrended topography).

High correlations are found between NIR albedo and thermal BT with a R^2 up to 0.67 (95% confidence interval) and between SPWD versus NIR albedo and thermal BT ($R^2 = 0.44$ and 0.57 at 95% confidence interval, respectively) calculated along all the transects (Fig. 3). The comparison between thermal BT and SPWD shows the same pattern observed for the NIR albedo, but proportionally inverse with respect to SPWD (Fig. 3), with higher temperatures corresponding to the glazed part of downwind areas of the dunes and conversely, lower values related to snow sastrugi in the upwind zones.

Based on the transects, the variability in NIR albedo at seasonal (spring-summer) to plurianual scale is observed to be twice as large in the snow accumulation area on the upwind flank and the bottom of the leeward flank (Fig. 2) compared to the glazed

surface NIR albedo (0.7% compared to 0.3% NIR albedo variability), which remains more stable and more highly correlated at seasonal (spring-summer) and pluriannual scale.

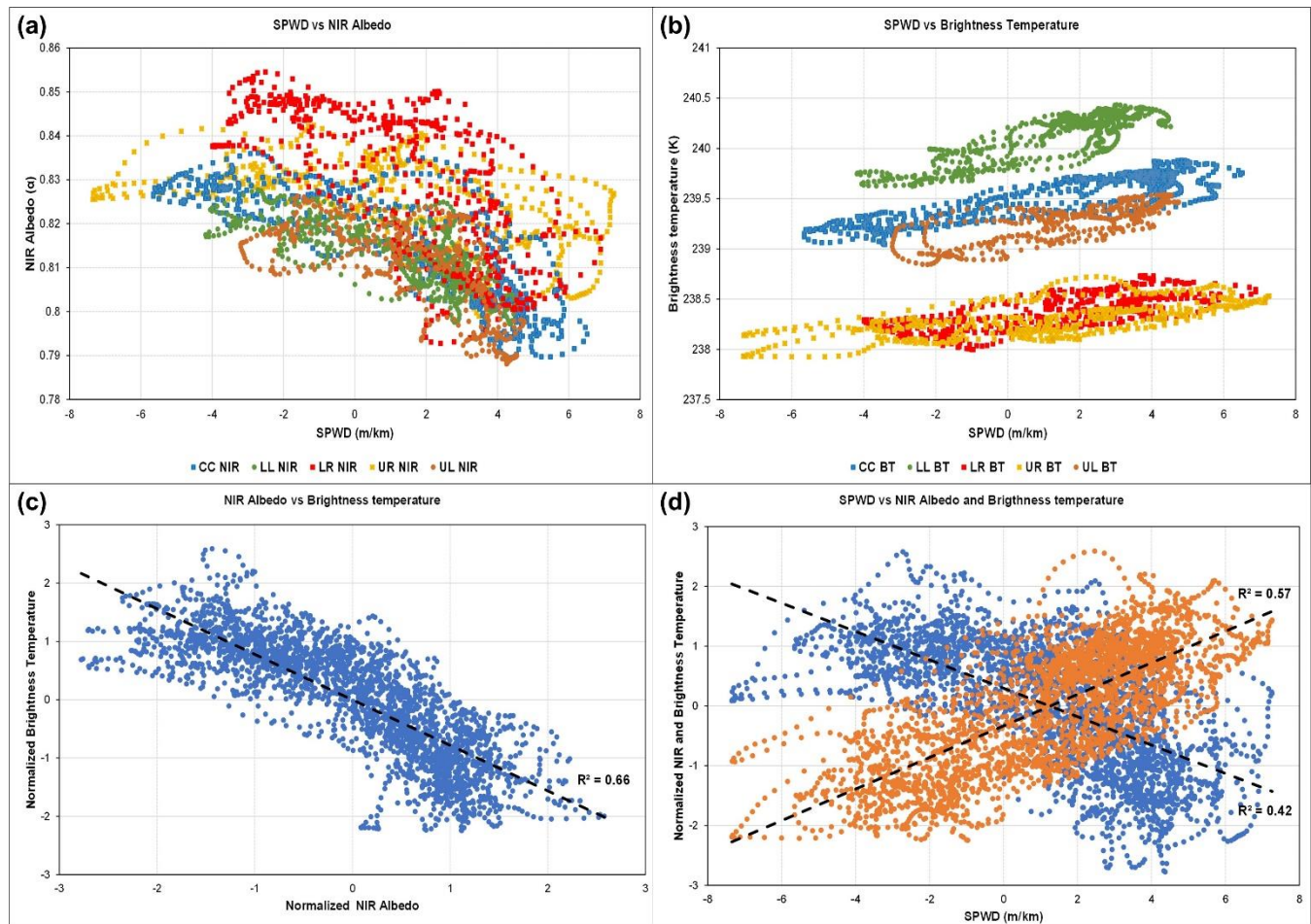


Figure 3: Diagram plots of transects at the EAIIST site from a Landsat 8 image acquired on 25-Nov-2013: (A) SPWD (slope along the prevailing wind direction) compared within each transect (C, LL, LR, UL, UR; Fig. 1 for location) with NIR spectral albedo and (B) thermal BT; (C) normalised NIR albedo of all transects compared with BT with linear regression; (D) SPWD compared with normalised NIR albedo and thermal BT for all transects with linear regression.

The analysis of sastrugi direction using seven Landsat scenes from the spring and summer months during the period 2013-2020 show small differences in direction within each image and in repeated imagery ($< 5^\circ$), confirming the stability in direction of sastrugi landforms and thus the persistence of katabatic wind.

310 The comparison of the results of wind direction obtained using sastrugi direction by satellite (resampled using bilinear interpolation) and ERA5 present similar values for both areas, with lower difference in the EAIIST area (differences of 1° in average values) compared to It-ITASE (9-14°, see Table A3).

315 At the regional scale (30 km spatial resolution), the entire megadune field has an average SPWD of 1.2 m km⁻¹, when calculated using sastrugi-based wind direction, and 1.1 m km⁻¹ when using ERA5, in agreement with previous studies (e.g., Frezzotti et al., 2002b). To distinguish between leeward (glazed surface) and windward flanks of the dunes for the two sites, the SPWD based on sastrugi was further resampled to 120 m using bilinear interpolation. For the SPWD on megadunes at local scale (hundred meter), we found a mean value of 5.6±1.0 m km⁻¹ for the leeward side and negative SPWD values, with a mean of -4.2±1.6 m km⁻¹ on the windward flanks.

320 The application of the supervised classification and the self-defined-threshold methodology on the different combination of the analysed parameters, for the 2013-2014 season and on the 17/Dec/2015 scene showed contrasting results (Table 2).

Date	NIR	BT-SPWD	NIR-SPWD	NIR-BT	NIR-BT-SPWD
25-Nov-2013	32%	57%	55%	9%	55%
11-Dec-2013	27%	52%	50%	32%	55%
27-Dec-2013	9%	43%	50%	9%	45%
28-Jan-2014	23%	43%	45%	23%	50%
Season average	23 ± 9%	49 ± 6%	50 ± 3%	18 ± 10%	51 ± 4%
17-Dec-2015	78%	48%	83%	70%	78%

Table 2: accuracy assessment (%) in the detection of glazed snow using a supervised classification applied on NIR, BT and SPWD and their combination over the four scenes of 2013-2014 summer season and on 17-Dec-2015. The results of BT and SPWD (alone) are not reported, as they present the same result in all cases (i.e., 0% for BT and 30% for SPWD).

325 In fact, even if the general accuracy in distinguishing firn and glazed surfaces was on average high (mostly > 80%), with the highest values on the scene from 17-Dec-2015 (up to 94% and 98% in the combination of NIR-SPWD for supervised and self-defined thresholds respectively), lower values and higher differences were found when comparing the accuracy in detecting only glazed snow. There, the inclusion of SPWD in the classification significantly improves the ability to detect these surfaces, 330 with a doubling of the accuracy during the season 2013-2014 (between 0% and 30% for single parameters or combination without SPWD, to around 50% of season average in the other cases, and up to 55% for NIR-BT-SPWD combination). The increase is also observed for the 17-Dec-2015 scene, from 78% of NIR alone to 83% for NIR-SPWD (which becomes 95% in the case of NIR-SPWD for self-defined-threshold methodology, the highest calculated value of accuracy in detecting glazed snow). Summarizing, the impact of the inclusion of the SPWD is evident, both applying the supervised classification and self-defined-threshold methodology, as the SPWD doubles the accuracy compared to the cases with no SPWD. We further observed 335

issues in using BT in these approaches, because of its high heterogeneity at high scale (i.e., entire Landsat scene), as BT presents strong variations across the image; the strong improvement in using a scene (i.e., 17-Dec-2015) with no interferences (e.g., fog, clouds, “low” SZA) and close in time to the REMA DEM (stripes from January to October 2016), leading to a significant increase in accuracy of the method (from highest values of ~ 50% of scenes from season 2013-2014 to over 80%); and the higher accuracy when applying a self-defined-threshold approach.

3.2 Megadune migration

The absolute megadune movement calculated using feature tracking on optical satellite image pairs spans from 3 to 6 years and presents small differences in the two study areas, ranging between 10.5 m a^{-1} and 14.2 m a^{-1} overall, with no detected significant trends over time. The average values are similar when using different datasets (Landsat 8 OLI and Sentinel-2), but with Sentinel-2 velocities showing slightly lower average values compared to Landsat 8. Moreover, due to the slightly higher spatial resolution (10 m versus 15 m), the number of features tracked using Sentinel-2 are an order of magnitude higher than those of Landsat 8 OLI (Table 1). The direction of the migration does not differ much across the different datasets, showing opposite values compared to wind direction. The second method used to calculate the migration velocity is the ridge vectorization and tracking for the same image pairs. This method shows slightly higher velocities ($16.7 \pm 3 \text{ m a}^{-1}$) than IMCORR tracking of megadune features ($11.9 \pm 3.6 \text{ m a}^{-1}$) at the EAIIST site for the period 2013-2019, but within the error.

At the D6 It-ITASE site, five GPS-GPR transects were surveyed on megadunes (Frezzotti et al., 2002b); the comparison between GPS elevations (3-Jan-1999) and REMA DEM (02-Feb-2014) provides information about the relative change in elevation at high resolution (decametre level) of the megadunes during the past 15 years. On the 5 transects, we observe an almost stable elevation in correspondence with glazed surface/leeward flank, whereas the maximum difference in elevation (from +1.2 to +1.9 m, with an average maximum value of +1.4 m) occurs always in the snow accumulation/upwind flank on the correspondence of the trough (Fig. 4). By projecting the transects along the prevalent wind direction (239°), based on the surrounding sastrugi orientation, we were able to evaluate the megadune migration using the relative change in elevation. Using the crest/trough position of each dune, we calculated an average displacement of $11 \pm 5.2 \text{ m a}^{-1}$ from all transects (Fig. 4). The migration of the dunes is evident in all transects with the upwind migration of the crest over the upstream flank and of the trough on the upstream flank of the previous megadune. In contrast, the glazed surfaces on the downwind flank remained generally stable in elevation over time (Fig. 4) but are clearly buried at the upstream flank foot and migrate at the crest. At the D6 site, Vittuari et al. (2004) measured an ice velocity of $1.46 \pm 0.04 \text{ m a}^{-1}$ with a direction of 97° using repeated GPS measurement between 1999 and 2001. The closer value of MEASUREs ice flow at the D6 site is $2.2 \pm 1.1 \text{ m a}^{-1}$ with a direction of 89° , in agreement with GPS measurements. At the EAIIST site, MEASUREs data show an ice flow of $6.1 \pm 3.4 \text{ m a}^{-1}$ with a direction of $\sim 65^\circ$. Both velocity directions agree with the topographic slope at the site. Applying Eq. (1) for the calculation of megadune-migration components, we obtained a sedimentological migration of $18.4 \pm 6.7 \text{ m a}^{-1}$ (229°) at EAIIST and $15.4 \pm 4.7 \text{ m a}^{-1}$ (246°) at It-ITASE using Landsat 8 OLI data, and $16.0 \pm 7.3 \text{ m a}^{-1}$ (230°) at EAIIST and $13.6 \pm 4.9 \text{ m a}^{-1}$ (245°) at It-ITASE with Sentinel-2.

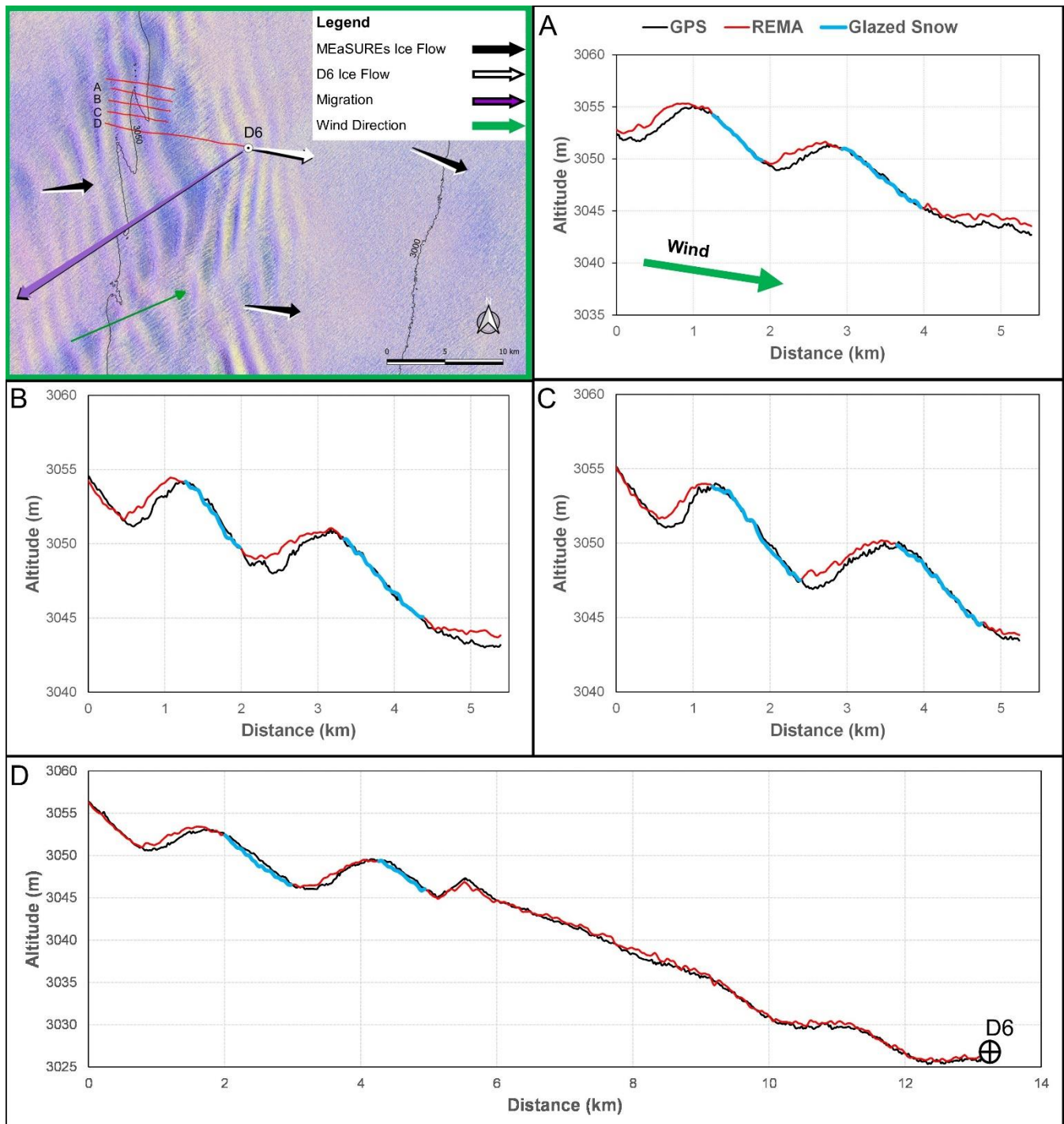


Figure 4: Location of the GPS transects (red) at the It-ITASE site with false colour Landsat 8 OLI image in background (18/Dec/2014). Universal Transverse Mercator (UTM) projection. Topographic section of four transects (A-B-C-D), with the black

lines representing elevation from in situ GPS observations (1999), red lines from REMA DEM (2014) and blue lines glazed snow detected on Landsat image from 18-Dec-2014.

4 Discussion

375

4.1 Application of the automatic detection of glazed snow on megadune fields

380

In this study, we showed the possibility to calculate the SPWD based on wind direction from ERA5 and Landsat-derived sastrugi. At both investigated sites, the direction of the wind from ERA5 at velocity higher than 11 m s^{-1} was found to be closer to the direction of sastrugi surveyed by satellite. The small difference between the two datasets could be correlated to the formation of sastrugi, as wind speed $\geq 11 \text{ m s}^{-1}$ was previously reported by Kodama et al. (1985) and Wendler et al. (1993) to be required for the formation of sastrugi. While the EAIIST site shows similar average directions to ERA5, in the other study area (It-ITASE) a slightly higher difference was found between the two datasets for wind velocity slower than 11 m s^{-1} . The direction retrieved from Landsat is strongly dependent on high velocity prevailing winds (katabatic winds), that shape the sastrugi and direction, while ERA5 also takes into account other wind directions than the katabatic. In addition, this difference could be caused by the different spatial and temporal resolutions between the satellite and ERA5 (30 m vs 30 km, scene-based vs average of 20 years), as well as inaccuracies in the ERA5 wind direction. The larger difference in wind direction using the various datasets (ERA5, sastrugi detected by satellite, sastrugi measured on the field) at It-ITASE site could also be attributed to the higher variability of the katabatic wind direction; in fact, this site is at the northern limit of megadune field (Fig. 1), and a relatively high variability of katabatic wind direction ($>10-15^\circ$) could be among the threshold factors that does not allow the formation of megadunes in the northern part. However, with the aim of applying this methodology at large-scale using ERA5 data, e.g., the whole continent, the differences between the two sources can be significant (e.g., at the It-ITASE site), and could produce errors in the SPWD calculation. Therefore, the use of sastrugi could be a more accurate way to interpret prevalent wind direction with high wind speed ($\geq 11 \text{ m s}^{-1}$) compared to ERA5.

390

395

The SPWD is the only parameter that could be considered as almost constant at 10s km scale, in consideration of the stability of the direction of the katabatic wind, driven mainly by surface slope and the Coriolis force. In contrast, albedo and above all thermal BT change both temporally, annually and during seasons and spatially across the satellite scene. In fact, NIR albedo significantly varies because of surface changes up to 0.1α and between the beginning, the middle and end of the summer season in relation to the SZA by $\pm 0.01-0.02 \alpha$. Frezzotti et al., (2002b) pointed out the presence of huge sastrugi (up to 1.5 m in height) located on the windward flank and alternation of sastrugi (up to 40 cm) and glazed surfaces located at the bottom of the interdune area. The observed change on NIR albedo and BT on the windward flank is correlated to the sastrugi formation and deterioration during the season, and their relative change in shadow (Warren, 1982). In addition, thermal BT varies from a higher temperature near the summer solstice to lower values in late spring and summer, in the range $\pm 5-10^\circ\text{K}$. In both cases, the differences between leeward flanks where glazed surfaces are located and windward flanks of megadunes are not high enough to overcome the seasonal variability and thus a constant range for albedo and temperature is impossible to determine.

405 Spatially, the satellite derived NIR and thermal BT show large variability inside the same satellite images, in particular for thermal BT, but strong correlation among the two parameters up to a R^2 of 0.99 along each transect. The observed variabilities could be related to the different illumination condition and meteorological conditions with development of surface hoar crystal due to fog and under calm sunny weather with a downward as well as an upward vapour source to the near-surface layer. The growth of surface hoar crystals dramatically changes the snow structure, specific surface area, and density, as well as surface roughness, leading to significant changes in albedo and therefore surface temperature (Gallet et al., 2014). For these reasons, 410 different thresholds can be required when investigating an entire tile of Landsat in the case of self-defined-threshold methodology, but can also explain the inability of supervised classification based only on BT to distinguish between glazed snow and firn. With BT, in fact, the difference in values across the images is higher than the mean spectral difference between these two surfaces at these wavelengths. For the same reasons, the classification approaches including BT present, in most cases, lower accuracy than the other cases, suggesting against using it to map glazed snow at large scale. On the other hand, 415 NIR albedo does not show this sort of problem and instead demonstrates good ability in distinguishing between the two surfaces, with a good accuracy even when used alone (especially in 17-Dec-2015 case, Table 2). Additionally, it is evident how the implementation of SPWD is fundamental in aiding the detection of glazed snow, together with the NIR band, particularly by improving the detection even when the other parameters present more uncertainties (owing to e.g., SZA, fog, etc.). In fact, in all the combinations where SPWD is included, the accuracy in the distinction between glazed snow and firn 420 shows more constant results and minimum and maximum accuracy across the analysed season is similar. Finally, our results point out the importance of using satellite images with no interferences (e.g., clouds, fog, high SZA), with the aim of automatically detecting glazed snow, as the accuracy of the method drastically increases (17-Dec-2015 compared to the other cases) and also that the self-defined-threshold approach provides better results in terms of accuracy than the supervised classification. Nevertheless, even if the self-defined-threshold model shows a higher accuracy, supervised classification allows 425 to overcome the issue of defining accurate thresholds across a certain season, providing good accuracy results especially on good quality images, as calculated on 17-Dec-2015.

430 By using the classifications with the highest accuracy in the EAIIST area achieved based on the scene from 17-Dec-2015 (NIR-SPWD combination), where approximately 75% of the area is covered by megadunes, we could calculate that the glazed surfaces cover around 43% of this specific dune area, i.e., ~ 80% of leeward flanks.

435 In conclusion, the detection of glazed surface/ablation area by satellite images is challenging because of differences in illumination and meteorological conditions (cloud cover, blowing snow etc.) among different satellite images. Nevertheless, the high resolution digital terrain model (REMA) allows to calculate a SPWD with unprecedented detail, similar to the resolution of optical satellites (Landast 8-9, Sentinel), and significantly improves the detection of glazed/ablation surfaces at ten-meter scale across the continent; therefore, it could significantly improve research on the SMB of the Antarctic Ice Sheet.

435

4.2 Megadune upwind migration

The absolute position of the megadune crest and trough are driven mainly by two processes: snow ablation/accumulation processes and ice sheet surface flow. GPS and GPR profiles along the It-ITASE traverse show the presence of paleo-megadunes buried up to the investigation depth of 20 m (Frezzotti et al., 2002b). Analysis of the D6 firn core allowed to detect the Tambora

440 eruption signal (1816 AD) at 15.36 m depth with an average snow accumulation of $36 \pm 1.8 \text{ mm w.e. a}^{-1}$, whereas an average value of $29 \pm 7 \text{ mm w.e. a}^{-1}$ of spatial variability in SMB at D6 site was evaluated by GPR calibrated using accumulation at three firn cores (Frezzotti et al., 2005). The elevation changes during 15 years observed using GPS and REMA show a relative increase of accumulation on the windward flank with the maximum value at the trough compared to the glazed surface area from 29 to 46 mm w.e. a^{-1} with an average value of 34 mm w.e. a^{-1} , using a density of 360 kg m^{-3} in the first two metres. This 445 value is very close to the estimated change of accumulation in the megadune area from 7 to 35 mm w.e. a^{-1} provided by Frezzotti et al., (2002b) using the variability of GPR internal layering at the megadune site. The minimum value represents a decrease in accumulation up to 75% or more on glazed surfaces. The relative stability of glazed surfaces with respect to elevation change and NIR albedo confirms the extremely stable SMB low value of the glazed surfaces with respect to accumulation areas, due to the long-term hiatus in SMB forced by wind scouring processes.

450 Using the isochrone distance of 1.5-1.8 km between the 180 years old paleo-crest detected by GPR and the recent crest from GPS observations (1998-99 AD), we can evaluate the windward migration of the paleo megadune crest at about $8-10 \text{ m a}^{-1}$. This vector from field observations summed with an ice flow from GPS of $1.46 \pm 0.04 \text{ m a}^{-1}$ with a direction of 97° produced an absolute migration of 10.3 m a^{-1} with a direction of 214° . This value is in very good agreement with absolute migration calculated using the elevation comparison between GPS and REMA ($11 \pm 5.2 \text{ m a}^{-1}$) and with satellite tracking (from 11.4 to 455 14.0 m a^{-1}), in particular with Sentinel-2 images (11.4 m a^{-1} , Table 1). At the D6 site, the movement components show different intensity with an order of magnitude of difference: $1-2 \text{ m a}^{-1}$ for ice flow, versus $13.6-15.4 \text{ m a}^{-1}$ for sedimentological migration. The components present nearly opposite directions: 97° for ice flow and 245° for sedimentological migration. The results 460 allowed us to calculate all the components of migration and to conclude that for a megadune with a wavelength of 3 km we could calculate an absolute migration of approximately 10 m a^{-1} . This burying process of snow on glazed surfaces takes about 300 years, with overlap of crest to through and glazed to sastrugi surface as observed by GPR internal layering.

The megadune migration on the upwind part observed by elevation change and tracking is also confirmed by the comparison of NIR and BT along the studied transects. These parameters remain relatively stable during the observed time on the glazed surface on the leeward flank, whereas the positive SMB upwind flank and bottom through area change significantly at pluriannual scale, but also at seasonal scale. Hence, we observe a general overestimation of sedimentological and absolute 465 migration using remote sensing with a mean difference of $+1.9 \text{ m a}^{-1}$ for Sentinel-2 (uncertainties of 19% for sedimentological migration and 10% for absolute migration). Using Landsat 8 OLI images, larger differences were found, with an average overestimation of 3.8 m a^{-1} . This difference could be caused by spatial variability of processes: with remote sensing we analysed a much wider area, as opposed to in situ observations which were acquired in transects on a limited section of the

megadune field. Finally, the spatial resolution and geolocation (Mouginot et al., 2017) could affect the satellite data, as
470 demonstrated by the worse results obtained using Landsat images at 15 m spatial resolution against 10 m of Sentinel-2.

The ice velocity of MEaSUREs is based on SAR images and is in very good agreement with GPS measurement, and the
475 tracking methods of IMCORR using optical images and crest displacement is in agreement with the migration of morphologies
observed from the comparison between change in elevation by GPS and REMA. Based on our analysis, the sedimentological
processes are analogous at It-ITASE and EAIIST sites. At the second site, a faster ice-flow motion was observed by
475 MEaSUREs, and the velocity of absolute migration is reduced by almost 35%, compared to the initial sedimentological-
migration velocity.

The ice velocity based on SAR images presents a phase centre that penetrates up to 10 m on dry and cold firn (Rignot et al.,
2001) and provides information on ice flow and not surface features. In contrast, using feature tracking on optical images
480 (Landsat and Sentinel-2), it is possible to estimate the absolute migration (migration + ice flow) of surface features that could
be significantly different from ice flow as for the megadunes.

5 Conclusions

This study significantly improved the previous knowledge on the temporal/spatial variability of Antarctic megadunes and
485 glazed surfaces, measurements of their sedimentation/migration and their interaction with atmosphere and ice sheet surface.
The snow accumulation distribution/variability processes that allow megadune formation have important consequences
concerning the choice of sites for ice coring and SMB evaluation, since orographic variations of few metres per kilometre have
485 a significant impact on the snow accumulation process. Furthermore, these new results represent a new ground truth and
foundation of knowledge for ice sheet mass balance research, in particular for satellite altimeter and ice velocity derived by
remote sensing measurements (e.g., radar vs optical/lidar).

The new results confirm and quantify the previous hypotheses and provide new relevant information on different aspects of
490 these peculiar landforms showing that the megadune is a dynamic feature at different spatial and temporal scales.

The glazed surface/megadune survey has revealed previously unknown large spatial variability in ice sheet SMB,
superimposed on the large/scale gradients in SMB from the coast to the interior. On smaller scales (<1 km), SMB varies
495 considerably as well, driven by surface topography undulations (SPWD) and consequent wind-driven snow ablation and
redistribution, which challenges the spatial representativeness of stake and firn/ice core records. Moreover, this small-scale
variability is not represented by Regional Climate Model systems used for SMB evaluation (eg. Agosta et a., 2019; Lenaerts
et al., 2019), which currently operate at horizontal resolutions of typically 25 km for East Antarctica. Previous studies have
500 pointed out that glazed areas are extensive enough to have a significant impact on current estimates of SMB, and therefore
overall mass balance using the mass budget method (Frezzotti et al., 2004; Das et al., 2013; Scambos et al., 2012). The scale
of the overestimation is of the same order of magnitude as the total error reported for East Antarctica and a large fraction of
the currently reported error bars for Antarctic-wide mass balance (Rignot et al., 2019).

Considering the characteristics of megadunes, the leeward glazed flanks show a lower NIR albedo (up to 0.1) and higher BT (up to 1.5 K) compared to windward snow-covered sides within each of the five transects analysed. NIR albedo and thermal BT, combined with the SPWD, allowed us to produce a method for automatically detecting glazed surfaces. High correlations were found between SPWD and NIR albedo and thermal BT with a R^2 up to 0.44 and 0.57 respectively calculated along the 505 whole transect examined in 2013-14, with differences between spring and end of summer. The correlations between SPWD and NIR albedo on the transects decrease to 0.39 in comparison with the image from Dec 2019. Moreover, the high correlation of NIR albedo between images decreases over time by up to 60% between Nov 2013 and Dec 2019. Our results support the importance of SPWD (especially when sufficiently synchronous with spectral imagery, in consideration of the migration of megadunes) for megadune snow characterization. Together with NIR albedo, the SPWD was found to be more important than 510 BT in the classification, and to provide a higher accuracy than spectral data only, by allowing accuracy >80% in detecting glazed snow. Further research might consider other parameters to automatically detect snow glazed surfaces, including snow grain size or the normalised difference snow index.

Finally, we provided for the first time an estimation of megadune migration from field and remote observations at the It-ITASE site. The results obtained using field measurements and remote observations allow to calculate all the components of megadune 515 migration, absolute ($11\text{-}14 \text{ m a}^{-1}$), sedimentological migration ($13\text{-}15 \text{ m a}^{-1}$) and the ice flow ($1\text{-}2 \text{ m a}^{-1}$) and to conclude that for a megadunes with a wavelength of 3 km and migration of approximately 10 m a^{-1} , the burying process of snow on glazed surfaces takes about 300 years, with overlap of crest to through and glazed to sastrugi surface.

The reconstruction of paleoclimate based on firn/ice cores drilled in megadune or downstream area is very complex; the distortion of recordings is characterised by a snow accumulation/hiatus periodicity of about hundreds of years. The length of 520 periodic variations due to mesoscale relief and/or megadunes depends on ice velocity, megadune migration and snow accumulation, and can therefore vary in space and time within the $500,000 \text{ km}^2$ of megadune field and downstream area. In the end, our work points out the importance of “antidunal” sedimentological processes in megadune fields with an almost opposite direction between the migration of surface features and ice flow derived respectively from feature tracking of optical images and SAR. These results present significant implication for surface measurements using Radar/Lidar altimetric satellite 525 and measurements of ice flow using optical and SAR image in the megadune area. Moreover, our results point out the different elevation behaviour at pluriannual scale of the stable elevation and NIR albedo of glazed surface, while the snow-covered surface changes elevation and NIR albedo, with a higher accumulation/elevation in correspondence with the previous trough, decreasing from the trough towards the windward crest. Wind-driven process greatly affects the SMB of the megadune area, which implies that all or most of the regional accumulation (as determined by RACMO and other models) is gathered in the 530 accretionary faces whereas in the downwind area the SMB is near zero with a long hiatus in snow accumulation.

Data availability

Data used to the aims of the present study are available from different repositories: Landsat 8 and Sentinel 2 imagery are available from <https://earthexplorer.usgs.gov/>; ERA5 data are available from <https://www.ecmwf.int/en/forecasts/datasets/reanalysis-datasets/era5> and REMA DEM from <https://www.pgc.umn.edu/data/rema/>. Field data were obtained from previously published papers, i.e., Frezzotti et al. (2002a, b) and Vitturari et al. (2004).

Author contributions

GT, MF conceived the idea of this work. GT and DF developed the procedure and processed the satellite image and data. All authors contributed to the writing of the final manuscript.

Competing interests

The authors declare that they have no conflict of interest.

Acknowledgments

The authors are thankful to PNRA- National Antarctic Research Program and MNA-National Antarctic Museum-of Italy (respectively fellowship and PhD Scholarship of G. Traversa), the Department for Regional Affairs and Autonomies (DARA) of the Italian Presidency of the Council of Ministers and Levissima Sanpellegrino S.p.A. (post-doc fellowship of D. Fugazza). This study was supported by the EAIIST project (ANR-16-CE01- 0011), the Institut Polaire Français Paul-Emile Victor (IPEV), the National Antarctic Research Program (PNRA), the French Research National Agency (Project). The authors would like to warmly thank all the participants of the It-ITASE and EAIIST traverses for their tremendous field contributions allowing the collection of the crucial in situ measurements used in this study.

References

Agosta, C., Amory, C., Kittel, C., Orsi, A., Favier, V., Gallée, H., van den Broeke, M. R., Lenaerts, J. T. M., van Wessem, J. M., van de Berg, W. J., and Fettweis, X.: Estimation of the Antarctic surface mass balance using the regional climate model MAR (1979–2015) and identification of dominant processes, *The Cryosphere*, 13, 281–296, <https://doi.org/10.5194/tc-13-281-2019>, 2019.

Albert, M., Shuman, C., Courville, Z., Bauer, R., Fahnestock, M., and Scambos, T.: Extreme firn metamorphism: impact of decades of vapor transport on near-surface firn at a low-accumulation glazed site on the East Antarctic plateau, *Ann. Glaciol.*, 39, 73–78, <https://doi.org/10.3189/172756404781814041>, 2004.

Arcone, S. A., Jacobel, R., and Hamilton, G.: Unconformable stratigraphy in East Antarctica: Part I. Large firn cosets, recrystallized growth, and model evidence for intensified accumulation, *J. Glaciol.*, 58, 240–252, <https://doi.org/10.3189/2012Jo11J044>, 2012a.

Arcone, S. A., Jacobel, R., and Hamilton, G.: Unconformable stratigraphy in East Antarctica: Part II. Englacial cosets and recrystallized layers, *J. Glaciol.*, 58, 253–264, <https://doi.org/10.3189/2012JoG11J045>, 2012b.

565 Azzoni, R. S., Senese, A., Zerboni, A., Maugeri, M., Smiraglia, C., and Diolaiuti, G. A.: Estimating ice albedo from fine debris cover quantified by a semi-automatic method: the case study of Forni Glacier, Italian Alps, *The Cryosphere*, 10, 665–679, <https://doi.org/10.5194/tc-10-665-2016>, 2016.

Bishop, M. P., Björnsson, H., Haeberli, W., Oerlemans, J., Shroder, J. F., and Tranter, M.: *Encyclopedia of snow, ice and glaciers*, Springer Science & Business Media, 2011.

Canny, J.: A computational approach to edge detection, *IEEE Trans. Pattern Anal. Mach. Intell.*, 679–698, 1986.

570 Courville, Z. R., Albert, M. R., Fahnestock, M. A., Cathles, L. M., and Shuman, C. A.: Impacts of an accumulation hiatus on the physical properties of firn at a low-accumulation polar site, *J. Geophys. Res.*, 112, F02030, <https://doi.org/10.1029/2005JF000429>, 2007.

575 Dadic, R., Mott, R., Horgan, H. J., and Lehning, M.: Observations, theory, and modeling of the differential accumulation of Antarctic megadunes: ACCUMULATION OF ANTARCTIC MEGADUNES, *J. Geophys. Res. Earth Surf.*, 118, 2343–2353, <https://doi.org/10.1002/2013JF002844>, 2013.

Das, I., Bell, R. E., Scambos, T. A., Wolovick, M., Creyts, T. T., Studinger, M., Frearson, N., Nicolas, J. P., Lenaerts, J. T. M., and van den Broeke, M. R.: Influence of persistent wind scour on the surface mass balance of Antarctica, *Nat. Geosci.*, 6, 367–371, <https://doi.org/10.1038/ngeo1766>, 2013.

580 Ekaykin, A. A., Lipenkov, V. Ya., and Shibaev, Yu. A.: Spatial Distribution of the Snow Accumulation Rate Along the Ice Flow Lines Between Ridge B and Lake Vostok, *Ice Snow*, 52, 122, <https://doi.org/10.15356/2076-6734-2012-4-122-128>, 2015.

Fahnestock, M. A., Scambos, T. A., and Bindschadler, R. A.: Semi-automated ice velocity determination from satellite imagery, *Eos*, 73, 493, 1992.

585 Fahnestock, M. A., Scambos, T. A., Shuman, C. A., Arthern, R. J., Winebrenner, D. P., and Kwok, R.: Snow megadune fields on the East Antarctic Plateau: Extreme atmosphere-ice interaction, *Geophys. Res. Lett.*, 27, 3719–3722, <https://doi.org/10.1029/1999GL011248>, 2000.

Foga, S., Scaramuzza, P. L., Guo, S., Zhu, Z., Dilley Jr, R. D., Beckmann, T., Schmidt, G. L., Dwyer, J. L., Hughes, M. J., and Laue, B.: Cloud detection algorithm comparison and validation for operational Landsat data products, *Remote Sens. Environ.*, 194, 379–390, <https://doi.org/10.1016/j.rse.2017.03.026>, 2017.

590 Frezzotti, M., Gandolfi, S., Marca, F. L., and Urbini, S.: Snow dunes and glazed surfaces in Antarctica: new field and remote-sensing data, *Ann. Glaciol.*, 34, 81–88, <https://doi.org/10.3189/172756402781817851>, 2002a.

Frezzotti, M., Gandolfi, S., and Urbini, S.: Snow megadunes in Antarctica: Sedimentary structure and genesis, *J. Geophys. Res. Atmospheres*, 107, ACL 1-1-ACL 1-12, <https://doi.org/10.1029/2001JD000673>, 2002b.

595 Frezzotti, M., Pourchet, M., Flora, O., Gandolfi, S., Gay, M., Urbini, S., Vincent, C., Becagli, S., Gragnani, R., and Proposito, M.: New estimations of precipitation and surface sublimation in East Antarctica from snow accumulation measurements, *Clim. Dyn.*, 23, 803–813, <https://doi.org/10.1007/s00382-004-0462-5>, 2004.

Frezzotti, M., Pourchet, M., Flora, O., Gandolfi, S., Gay, M., Urbini, S., Vincent, C., Becagli, S., Gragnani, R., and Proposito, M.: Spatial and temporal variability of snow accumulation in East Antarctica from traverse data, *J. Glaciol.*, 51, 113–124, <https://doi.org/10.3189/172756505781829502>, 2005.

600 Fugazza, D., Senese, A., Azzoni, R. S., Maugeri, M., and Diolaiuti, G. A.: Spatial distribution of surface albedo at the Forni Glacier (Stelvio National Park, Central Italian Alps), *Cold Reg. Sci. Technol.*, 125, 128–137, <https://doi.org/10.1016/j.coldregions.2016.02.006>, 2016.

605 Fujii, Y., Yamanouchi, T., Suzuki, K., and Tanaka, S.: Comparison of the Surface Conditions of the Inland Ice Sheet, Dronning Maud Land. Antarctica. Derived from Noaa AVHRR Data with Ground Observation, *Ann. Glaciol.*, 9, 72–75, <https://doi.org/10.3189/S0260305500000410>, 1987.

Gallet, J. C., Domine, F., Savarino, J., Dumont, M., & Brun, E.: The growth of sublimation crystals and surface hoar on the Antarctic plateau, *The Cryosphere*, 8(4), 1205–1215, 2014.

610 Hersbach, H., Bell, B., Berrisford, P., Hirahara, S., Horányi, A., Muñoz-Sabater, J., Nicolas, J., Peubey, C., Radu, R., Schepers, D., Simmons, A., Soci, C., Abdalla, S., Abellán, X., Balsamo, G., Bechtold, P., Biavati, G., Bidlot, J., Bonavita, M., Chiara, G., Dahlgren, P., Dee, D., Diamantakis, M., Dragani, R., Flemming, J., Forbes, R., Fuentes, M., Geer, A., Haimberger, L., Healy, S., Hogan, R. J., Hólm, E., Janíková, M., Keeley, S., Laloyaux, P., Lopez, P., Lupu, C., Radnoti, G., Rosnay, P., Rozum, I., Vamborg, F., Villaume, S., and Thépaut, J.: The ERA5 Global Reanalysis, *Q. J. R. Meteorol. Soc.*, qj.3803, <https://doi.org/10.1002/qj.3803>, 2020.

615 Howat, I. M., Porter, C., Smith, B. E., Noh, M.-J., and Morin, P.: The Reference Elevation Model of Antarctica, *The Cryosphere*, 13, 665–674, <https://doi.org/10.5194/tc-13-665-2019>, 2019.

Jawak, S. D., Kumar, S., Luis, A. J., Bartanwala, M., Tummala, S., and Pandey, A. C.: Evaluation of geospatial tools for generating accurate glacier velocity maps from optical remote sensing data, in: Multidisciplinary Digital Publishing Institute Proceedings, 341, <https://doi.org/10.3390/ecrs-2-05154>, 2018.

620 Jezek, K. C.: Glaciological properties of the Antarctic ice sheet from RADARSAT-1 synthetic aperture radar imagery, *Ann. Glaciol.*, 29, 286–290, <https://doi.org/10.3189/172756499781820969>, 1999.

Klok, E. L., Gruell, W., and Oerlemans, J.: Temporal and spatial variation of the surface albedo of Morteratschletscher, Switzerland, as derived from 12 Landsat images, *J. Glaciol.*, 49, 491–502, <https://doi.org/10.3189/172756503781830395>, 2003.

625 Kodama, Y., Wendler, G., and Gosink, J.: The effect of blowing snow on katabatic winds in Antarctica, *Ann. Glaciol.*, 6, 59–62, <https://doi.org/10.3189/1985AoG6-1-59-62>, 1985.

Lenaerts, J. T., Medley, B., van den Broeke, M. R., and Wouters, B.: Observing and modeling ice sheet surface mass balance, *Rev. Geophys.*, 57, 376–420, 2019.

Liang, S.: Narrowband to broadband conversions of land surface albedo I: Algorithms, *Remote Sens. Environ.*, 76, 213–238, [https://doi.org/10.1016/S0034-4257\(00\)00205-4](https://doi.org/10.1016/S0034-4257(00)00205-4), 2001.

630 Mather, K. B.: Further observations on sastrugi, snow dunes and the pattern of surface winds in Antarctica, *Polar Rec.*, 11, 158–171, <https://doi.org/10.1017/S0032247400052888>, 1962.

Mayewski, P. and Goodwin, I.: Antarctic's role pursued in global climate change, *Eos Trans. Am. Geophys. Union*, 80, 398–400, <https://doi.org/10.1029/EO080i035p00398>, 1999.

635 Meredith, M., Sommerkorn, M., Cassotta, S., Derksen, C., Ekaykin, A., Hollowed, A., Kofinas, G., Mackintosh, A., Melbourne-Thomas, J., and Muelbert, M. M. C.: Polar Regions. Chapter 3, IPCC Special Report on the Ocean and Cryosphere in a Changing Climate, 2019.

640 Mouginot, J., Rignot, E., Scheuchl, B., and Millan, R.: Comprehensive annual ice sheet velocity mapping using Landsat-8, Sentinel-1, and RADARSAT-2 data, *Remote Sens.*, 9, 364, <https://doi.org/10.3390/rs9040364>, 2017.

Núñez-González, F. and Martín-Vide, J. P.: Analysis of antidune migration direction, *J. Geophys. Res. Earth Surf.*, 116, <https://doi.org/10.1029/2010JF001761>, 2011.

645 Palm, S. P., Yang, Y., Spinhirne, J. D., and Marshak, A.: Satellite remote sensing of blowing snow properties over Antarctica, *J. Geophys. Res.*, 116, D16123, <https://doi.org/10.1029/2011JD015828>, 2011.

Palm, S. P., Kayetha, V., Yang, Y., and Pauly, R.: Blowing snow sublimation and transport over Antarctica from 11 years of CALIPSO observations, *The Cryosphere*, 11, 2555–2569, <https://doi.org/10.5194/tc-11-2555-2017>, 2017.

650 Parish, T. R. and Bromwich, D. H.: Continental-scale simulation of the Antarctic katabatic wind regime, *J. Clim.*, 4, 135–146, [https://doi.org/10.1175/1520-0442\(1991\)004<0135:CSSOTA>2.0.CO;2](https://doi.org/10.1175/1520-0442(1991)004<0135:CSSOTA>2.0.CO;2), 1991.

Picard, G., Libois, Q., Arnaud, L., Verin, G., and Dumont, M.: Development and calibration of an automatic spectral albedometer to estimate near-surface snow SSA time series, *The Cryosphere*, 10, 1297–1316, <https://doi.org/10.5194/tc-10-1297-2016>, 2016.

655 Pietroni, I., Argentini, S., & Petenko, I.. One year of surface-based temperature inversions at Dome C, Antarctica. *Boundary-Layer Meteorology*, 150(1), 131–151, 2014.

Pirazzini, R.: Surface albedo measurements over Antarctic sites in summer, *J. Geophys. Res.*, 109, D20118, <https://doi.org/10.1029/2004JD004617>, 2004.

660 Proposito, M., Becagli, S., Castellano, E., Flora, O., Genoni, L., Gragnani, R., Stenni, B., Traversi, R., Udisti, R., and Frezzotti, M.: Chemical and isotopic snow variability along the 1998 ITASE traverse from Terra Nova Bay to Dome C, East Antarctica, *Ann. Glaciol.*, 35, 187–194, <https://doi.org/10.3189/172756402781817167>, 2002.

Prothero, D. R. and Schwab, F.: *Sedimentary geology*, Macmillan, 2004.

Rignot, E., Echelmeyer, K., and Krabill, W.: Penetration depth of interferometric synthetic-aperture radar signals in snow and ice, *Geophys. Res. Lett.*, 28, 3501–3504, <https://doi.org/10.1029/2000GL012484>, 2001.

665 Rignot, E., Mouginot, J., and Scheuchl, B.: MEaSUREs InSAR-based Antarctica ice velocity map, version 2, Boulder CO NASA DAAC Natl. Snow Ice Data Cent., 2017.

Rignot, E., Mouginot, J., Scheuchl, B., van den Broeke, M., van Wessem, M. J., and Morlighem, M.: Four decades of Antarctic Ice Sheet mass balance from 1979–2017, *Proc. Natl. Acad. Sci.*, 116, 1095–1103, <https://doi.org/10.1073/pnas.1812883116>, 2019.

670 Scambos, T. A., Dutkiewicz, M. J., Wilson, J. C., and Bindschadler, R. A.: Application of image cross-correlation to the measurement of glacier velocity using satellite image data, *Remote Sens. Environ.*, 42, 177–186, 1992.

Scambos, T. A., Frezzotti, M., Haran, T., Bohlander, J., Lenaerts, J. T. M., Van Den Broeke, M. R., Jezek, K., Long, D., Urbini, S., Farness, K., Neumann, T., Albert, M., and Winther, J.-G.: Extent of low-accumulation “wind glaze” areas on the East

670 Antarctic plateau: implications for continental ice mass balance, *J. Glaciol.*, 58, 633–647, https://doi.org/10.3189/2012JoG11J232, 2012.

Schaepman-Strub, G., Schaepman, M. E., Painter, T. H., Dangel, S., and Martonchik, J. V.: Reflectance quantities in optical remote sensing—Definitions and case studies, *Remote Sens. Environ.*, 103, 27–42, https://doi.org/10.1016/j.rse.2006.03.002, 2006.

Swithinbank, C.: *Antarctica*, US Government Printing Office, 1988.

675 Traversa, G., Fugazza, D., Senese, A., and Diolaiuti, G. A.: Preliminary results on Antarctic albedo from remote sensing observations, *Geogr Fis Din Quat*, 42, 245–254, http://dx.doi.org/10.4461/GFDQ.2019.42.14, 2019.

Traversa, G., Fugazza, D., Senese, A., and Frezzotti, M.: Landsat 8 OLI Broadband Albedo Validation in Antarctica and Greenland, *Remote Sens.*, 13, 799, https://doi.org/10.3390/rs13040799, 2021a.

680 Traversa, G., Fugazza, D., and Frezzotti, M.: Analysis of Megadune Fields in Antarctica, in: 2021 IEEE International Geoscience and Remote Sensing Symposium IGARSS, 5513–5516, https://doi.org/10.1109/IGARSS47720.2021.9554827, 2021b.

Traversa, G. and Fugazza, D.: Evaluation of Anisotropic Correction Factors for the Calculation of Landsat 8 OLI Albedo on the Ice Sheets, *Geogr Fis Din Quar*, 44, 91–95, http://dx.doi.org/10.4461/GFDQ.2021.44.8, 2021c.

685 Van Wessem, J. M., Reijmer, C. H., Morlighem, M., Mouginot, J., Rignot, E., Medley, B., Joughin, I., Wouters, B., Depoorter, M. A., Bamber, J. L., Lenaerts, J. T. M., Van De Berg, W. J., Van Den Broeke, M. R., and Van Meijgaard, E.: Improved representation of East Antarctic surface mass balance in a regional atmospheric climate model, *J. Glaciol.*, 60, 761–770, https://doi.org/10.3189/2014JoG14J051, 2014.

Vermote, E. F., Tanré, D., Deuze, J. L., Herman, M., and Morcette, J.-J.: Second simulation of the satellite signal in the solar spectrum, 6S: An overview, *IEEE Trans. Geosci. Remote Sens.*, 35, 675–686, https://doi.org/10.1109/36.581987, 1997.

690 Vittuari, L., Vincent, C., Frezzotti, M., Mancini, F., Gandolfi, S., Bitelli, G., and Capra, A.: Space geodesy as a tool for measuring ice surface velocity in the Dome C region and along the ITASE traverse, *Ann. Glaciol.*, 39, 402–408, https://doi.org/10.3189/172756404781814627, 2004.

Warren, S. G.: Optical properties of snow, *Rev. Geophys.*, 20, 67–89, https://doi.org/10.1029/RG020i001p00067, 1982.

Watanabe, O.: Distribution of surface features of snow cover in Mizuho Plateau, http://id.nii.ac.jp/1291/00000854/, 1978.

695 Wendler, G., André, J. C., Pettré, P., Gosink, J., and Parish, T.: Katabatic winds in Adélie coast, *Antarct. Meteorol. Climatol. Stud. Based Autom. Weather Stn.*, 61, 23–46, https://doi.org/10.1029/AR061p0023, 1993.

Zanter, K.: Landsat 8 (L8) data users handbook, *Landsat Sci. Off. Website*, 2019.

Appendix A

Sensor	Tile	Scene	Solar Zenith (deg)	Azimuth (deg)
OLI	069119	25-Nov-2013	69	89
OLI	069119	11-Dec-2013	67	91
OLI	069119	27-Dec-2013	67	93
OLI	069119	28-Jan-2014	72	95
OLI	069119	28-Nov-2014	68	89
OLI	069119	17-Dec-2015	67	92
OLI	069119	18-Jan-2016	70	95
OLI	069119	04-Nov-2017	74	87
OLI	069119	10-Nov-2019	72	88
OLI	069119	28-Dec-2019	67	93
OLI	069119	29-Jan-2020	73	95
OLI	081114	31-Oct-2014	68	62
OLI	081114	02-Dec-2014	61	65
OLI	081114	18-Dec-2014	60	67
OLI	081114	06-Jan-2016	62	69
OLI	081114	30-Nov-2019	62	65
OLI	081114	17-Jan-2020	64	70
S2	T51CWL	10-Jan-2018	67	87
S2	T51CWL	02-Jan-2021	66	84
S2	T52CEA	13-Dec-2016	59	59
S2	T52CEA	27-Dec-2020	59	61

Table A1. Landsat (OLI) and Sentinel-2 (S2) images in the EAIIST (069119 and T51CWL tiles for L8OLI and S2, respectively) and It-ITASE (081114 and T52CEA tiles for L8OLI and S2, respectively) areas used in the study with corresponding Solar Zenith and Azimuth angles from the Landsat/Sentinel Metadata.

	It-ITASE	EAIIST
--	----------	--------

Year	Nº of stripes	Percentage of the total	Nº of stripes	Percentage of the total
2008	5	0.4 %	5	0.5 %
2009	13	0.9 %	11	1.2 %
2010	27	1.9 %	27	2.9 %
2011	128	9.0 %	44	4.7 %
2012	27	1.9 %	16	1.7 %
2013	110	7.7 %	89	9.5 %
2014	217	15.2 %	184	19.6 %
2015	136	9.5 %	61	6.5 %
2016	593	41.6 %	398	42.5 %
2017	169	11.9 %	102	10.9 %

Table A2. Frequency of REMA DEM stripes at the EAIIST and It-ITASE sites from different years, based on the REMA strip index.

EAIIST		It-ITASE					
Dataset	Average	Max	Min	Dataset	Average	Max	Min
<i>Landsat 8</i>	224°	232°	212°	<i>Landsat 8</i>	240°	250°	215°
<i>ERA5</i> $\geq 0\text{m/s}$	225°	230°	220°	<i>ERA5</i> $\geq 0\text{m/s}$	227°	236°	215°
<i>ERA5</i> $\geq 3\text{m/s}$	225°	229°	220°	<i>ERA5</i> $\geq 3\text{m/s}$	226°	233°	217°
<i>ERA5</i> $\geq 5\text{m/s}$	225°	229°	220°	<i>ERA5</i> $\geq 5\text{m/s}$	226°	234°	217°
<i>ERA5</i> $\geq 7\text{m/s}$	225°	235°	220°	<i>ERA5</i> $\geq 7\text{m/s}$	227°	236°	218°
<i>ERA5</i> $\geq 11\text{m/s}$	223°	229°	216°	<i>ERA5</i> $\geq 11\text{m/s}$	231°	240°	223°

710 Table A3. Wind direction statistics (average, maximum and minimum values) for the considered datasets: Landsat 8 at 30 m spatial resolution and ERA5 at 30 km spatial resolution (divided into 5 sub-datasets according to wind speed) at the EAIIST and It-ITASE sites.